

Ferroelectric Skyrmions and a Zoo of Multiferroic Phases in GaV₄S₈

E. Ruff,^{1,*} S. Widmann,¹ P. Lunkenheimer,¹ V. Tsurkan,^{1,2} S. Bordács,³ I. Kézsmárki^{1,3} & A. Loidl¹

¹Experimental Physics V, Center for Electronic Correlations and Magnetism, University of Augsburg, 86135 Augsburg, Germany

²Institute of Applied Physics, Academy of Sciences of Moldova, Chisinau MD-2028, Republic of Moldova

³Department of Physics, Budapest University of Technology and Economics and MTA-BME Lendület Magneto-optical Spectroscopy Research Group, 1111 Budapest, Hungary

*Correspondence and requests for materials should be addressed to E.R. (email: eugen.ruff@physik.uni-augsburg.de).

The lacunar spinel GaV₄S₈ undergoes orbital ordering at 44 K and reveals a complex magnetic phase diagram below 13 K, including a ferromagnetic, cycloidal and Néel-type skyrmion lattice phase. Skyrmions are topologically protected nano-scale spin vortices with fascinating physical properties and high potential for future data storage. Here we provide a detailed study of the polar properties of GaV₄S₈, revealing that its orbitally ordered phase is ferroelectric with sizable polarization of $\sim 1 \mu\text{C}/\text{cm}^2$. Moreover, spin-driven excess polarizations emerge in all magnetic phases, hence, GaV₄S₈ hosts three different multiferroic phases including the skyrmion lattice formed by ferroelectric spin vortices. By taking into account the crystal symmetry and spin patterns of the magnetically ordered phases, exchange striction is identified as the main microscopic mechanism behind the spin-driven ferroelectric polarization in each multiferroic phase. The polar crystal structure of GaV₄S₈ is unique among the known skyrmion-lattice host materials and the ferroelectric SkL phase may be exploited for non-dissipative electric-field control of skyrmions.

Lacunar spinels, ternary chalcogenides of composition AM_4X_8 ($A = \text{Ga}$ and Ge ; $M = \text{V}, \text{Mo}, \text{Nb}$ and Ta ; $X = \text{S}$ and Se), represent an interesting class of transition-metal compounds with molecular clusters as structural building blocks^{1,2,3,4}. They can be derived from the normal spinel structure AM_2X_4 by removing every second A-ion from the tetrahedral site. Moreover, caused by a slight rearrangement of bond lengths due to an ordered defect formation, the structure consists of two weakly linked molecular units, cubane $(M_4X_4)^{n+}$ and tetrahedral $(AX_4)^{n-}$ clusters. Recently, a plethora of correlation effects has been reported for AM_4X_8 lacunar spinels, including pressure-induced superconductivity⁵, bandwidth-controlled metal-to-insulator transition^{6,7}, large negative magnetoresistance⁸, a two-dimensional topological insulating state⁹, resistive switching via an electric-field induced transition^{10,11,12}, emergence of orbitally driven ferroelectricity¹³ and an extended Néel-type skyrmion lattice (SkL) phase at low magnetic fields¹⁴.

The vanadium-derived lacunar spinel GaV₄S₈ is a magnetic semiconductor with non-centrosymmetric cubic T_d symmetry at room temperature^{15,16}. It consists of a network of weakly coupled $(V_4S_4)^{5+}$ cubane units forming a face centred cubic (fcc) lattice, separated by $(GaS_4)^{5-}$ tetrahedra (cf. inset of Fig. 1c). Each vanadium V_4 cluster can be characterized by a local spin $S = \frac{1}{2}$ (ref. 16). GaV₄S₈ undergoes a cubic-to-rhombohedral structural phase transition at $T_{IT} = 44$ K and magnetic ordering at $T_C = 13$ K (refs. 5, 17, 18). The low-temperature crystal structure has been described by the rhombohedral C_{3v} point group^{15,16}. The structural phase transition has been identified as a Jahn-Teller derived orbital ordering characterized by an elongation of the V_4 tetrahedra of the cubane units along one of the four crystallographic $\langle 111 \rangle$ directions¹⁹ (see inset of Fig. 1d). The structural transition creates a multi-domain state with submicron-thick sheets of the four different rhombohedral domains¹⁴. Ref. 14 has revealed a complex magnetic phase diagram of GaV₄S₈, with a cycloidal and SkL phase embedded within the FM state. Skyrmion lattices, periodic arrays of spin

vortices, have recently been observed in various magnets with chiral structure^{20, 21, 22, 23}. Most interestingly, in GaV₄S₈ novel Néel-type skyrmions, composed of spin cycloids carrying a monopole moment²⁴, have been identified¹⁴.

Here we report a detailed study of the ferroelectric (FE) properties of GaV₄S₈ as function of temperature and magnetic field, supplemented by specific heat and magnetic susceptibility measurements. We provide experimental evidence for the onset of ferroelectricity with sizable polarization at the Jahn-Teller transition at $T_{JT} = 44$ K. In addition, we find that the FE polarization is enhanced when crossing the magnetic phase boundaries, leading to different polarizations in the collinear FM, cycloidal and SkL phase. Based on the spin patterns in the three magnetically ordered phases and the symmetry of the V₄-V₄ bonds in the rhombohedral phase, we identify exchange striction as the microscopic origin of all spin-driven FE polarizations in GaV₄S₈ and estimate the corresponding exchange-striction parameters from the variation of the polarization between the different magnetic phases.

Results

Sample characterization. Figure 1 shows the temperature dependences of the main electronic and thermodynamic quantities measured in the vicinity and below the structural phase transition. In Fig. 1a, the magnetic susceptibility (open circles, left scale) shows a clear increase at low temperatures indicating the appearance of spontaneous magnetization as expected for a predominantly FM compound. At low temperatures and high external fields, the ordered moment is approximately 0.8 μ_B /f.u., close to the value expected for a spin $S = \frac{1}{2}$ system. The structural phase transition is clearly manifested in a jump of the inverse susceptibility (open squares, right scale) and a sharply peaked anomaly in the temperature dependence of the heat capacity (Fig. 1b: open squares, left scale), that allow locating the structural phase transition with high precision at $T_{JT} = 44.0$ K. The magnetic phase transition is also accompanied by a peak in the heat capacity at $T_C = 13$ K. These sharp anomalies also document the high quality of the single-crystalline material used in this work, which seems to be essentially impurity and strain free.

We estimated the electronic entropy by subtracting the phonon-derived heat capacity. The line in Fig. 1b has been calculated by assuming one Debye term for the acoustic modes and three Einstein terms for the remaining degrees of freedom. A good fit up to room temperature was obtained using a Debye temperature of 145 K and Einstein frequencies corresponding to 240 K, 450 K and 600 K. By subtracting the phonon part and integrating over the remaining excess heat capacity, we have determined the electronic entropy (open circles in Fig. 1b, right scale). The entropy change upon the magnetic transition is smaller than $R \ln 2$ that would correspond to the release of the full spin entropy in the paramagnetic (PM) phase. The entropy just above T_{JT} is approximately $1.43 R \ln 2$. This value is well below $R \ln 2 + R \ln 3 = 2.58 R \ln 2$, that is the total entropy associated with a single electron per V₄ unit occupying a triply degenerate orbital and carrying $S = \frac{1}{2}$. This entropy deficit likely indicates the presence of a dynamic Jahn-Teller effect in the cubic phase, namely the temporary deformation of V₄ units on the local scale²⁵. Static structural distortions lowering the symmetry from cubic T_d to rhombohedral C_{3v} are expected to occur via a first-order phase transition as odd power terms are allowed in the free energy of a non-centrosymmetric compound. Indeed, both the magnetic and structural transitions are accompanied by narrow hysteresis loops on heating and cooling. The first-order character of the structural phase transition could also hamper a precise determination of the entropy above T_{JT} .

Figure 1c shows the temperature dependence of the real part of the dielectric constant measured at 562 kHz. A significant anomaly appears at the Jahn-Teller transition, with a step-like increase and a subsequent continuous decrease of the dielectric constant below T_{JT} . We found that the magnitude of this dielectric anomaly is strongly frequency dependent and becomes increasingly suppressed at higher frequencies. At higher temperatures, the low-frequency dielectric constant is dramatically influenced by extrinsic Maxwell-Wagner like contributions, which arise from contact and surface effects and yield values of order 10^4 at room temperature^{26,27}. Such extrinsic contributions to the low-frequency

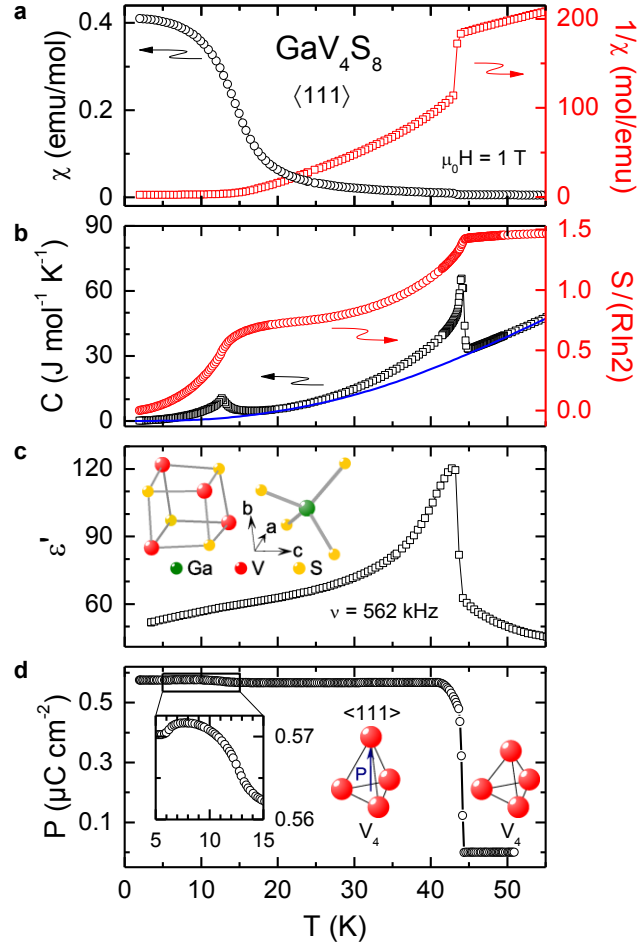


Figure 1 | Sample characterization. (a) Magnetic susceptibility $\chi = M/H$ (open circles, left scale) and inverse susceptibility (open squares, right scale) versus temperature measured in external magnetic fields of 1 T along the crystallographic $\langle 111 \rangle$ direction. (b) Temperature-dependent heat capacity C (open squares, left scale). The solid line represents an estimate of the phonon contribution to the heat capacity. The electronic entropy S , obtained by the integration of the specific heat after subtracting the phonon term, is indicated by open circles (right scale). (c) Real part of the dielectric constant ϵ' measured at 562 kHz (open squares). The electric field E was applied parallel to the crystallographic $\langle 111 \rangle$ direction. The inset shows the unit cell of GaV_4S_8 with the two molecular units, namely the V_4S_4 and GaS_4 clusters, and indicates the orientation of these molecular units with respect to the main cubic axes. (d) Electric polarization P vs. temperature measured parallel to the $\langle 111 \rangle$ direction. The elongation of the V_4 units along $\langle 111 \rangle$ below the Jahn-Teller transition is indicated. The inset shows the excess polarization at the onset of magnetic order.

dielectric constant are still present at T_{JT} ; hence, we restrict ourselves to relatively high frequencies where intrinsic dielectric constants are measured. The increase of the dielectric constant when approaching the Jahn-Teller transition from the cubic phase suggests the presence of polar fluctuations and clearly speaks against extrinsic effects. It seems quite natural to correlate these polar fluctuations with orbital fluctuations via a dynamic Jahn-Teller effect. Nevertheless, one has to keep in mind that the conductivity changes significantly at the structural phase transition with the onset of strong ac conductivity contributions¹⁷ just above T_{JT} , which can also influence the real part of the dielectric constant²⁷. Finally, the onset of magnetic order is hardly visible in the temperature dependence of the dielectric constant, only showing a small hump close to 13 K. It is worth mentioning that the temperature dependence of the dielectric constant in the FE and isostructural GeV_4S_8 also shows a very unusual behaviour¹³. A step-like increase occurs at the structural phase transition, which is followed by a step-like decrease at the subsequent magnetic transition. In the intermediate regime with enhanced dielectric constant, strong frequency dependence indicates significant ac conductivity¹³.

In GaV_4S_8 the FE polarization along the $\langle 111 \rangle$ direction, determined from pyrocurrent measurements, abruptly appears at the structural transition (see Fig. 1d), in agreement with the sharp

anomaly observed in the heat capacity. The polarization saturates somewhat below $0.6 \mu\text{C}/\text{cm}^2$, which is significantly larger than the polarization in spin-driven multiferroics^{28,29,30}, but by a factor of 50 lower than in canonical perovskite ferroelectrics³¹. This value is close to the FE polarization found in the related lacunar spinel GeV_4S_8 (ref. 13). In Fig. 1d we show the distortion of the vanadium tetrahedra along $\langle 111 \rangle$, being responsible for the macroscopic polarization. From the results presented in Fig. 1 it is clear that GaV_4S_8 is an improper orbital-order driven FE, where orbital order at the Jahn-Teller transition induces FE polarization. A closer inspection of Fig. 1d reveals an additional small step at the onset of magnetic order. The inset in Fig. 1d provides an enlarged view of the low-temperature polarization, which shows an increase upon entering into the cycloidal phase at 13 K and a small decrease close to 6 K when the low-temperature FM order is finally established¹⁴. This finding documents that in GaV_4S_8 in addition to the orbital-derived FE polarization of approximately $6000 \mu\text{C}/\text{m}^2$, an excess spin-driven polarization of the order of $100 \mu\text{C}/\text{m}^2$ appears in the magnetic phases. In the remaining part of this article, we focus on the most important and fascinating aspect of these results, namely the multiferroic nature of the different magnetically ordered phases, including the SkL phase with ferroelectric skyrmions.

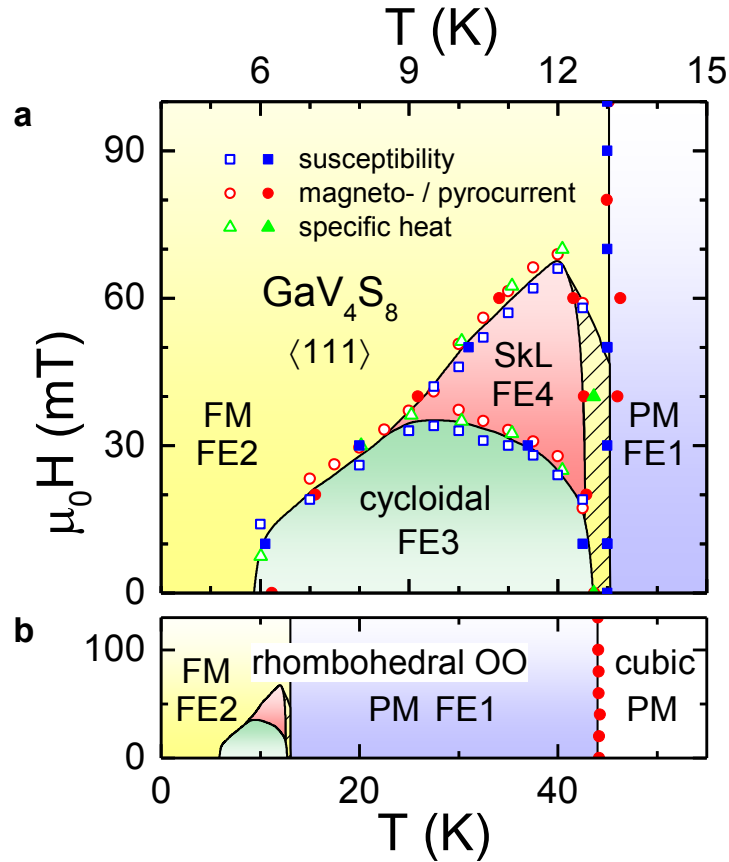


Figure 2 | Magnetic field versus temperature phase diagram of GaV_4S_8 for magnetic fields applied along one of the cubic $\langle 111 \rangle$ axes. (a) Low-temperature region below $T = 15$ K. The magnetic phase boundaries correspond to the unique structural domain whose easy axis is parallel to the magnetic field (for details see text). The SkL phase (red area) and the cycloidal phase (green area) are embedded within the FM phase (yellow area). Above $T_c = 13$ K the material is paramagnetic (PM). The phase boundaries as determined from magnetization, polarization (pyro- and magneto-current) and specific heat measurements are indicated by squares, circles and triangles, respectively. Full symbols correspond to temperature scans, while open symbols represent magnetic-field scans. The hatched area characterizes the regime between the paramagnetic and the cycloidal/SkL phase, where we cannot identify the exact spin structure. (b) Complete phase diagram extending beyond the Jahn-Teller transition. Below T_{JT} , within the orbitally ordered (OO) phase, four different FE states (FE1 – FE4) are found, each characterized by well distinguishable polarization.

Phase diagram of GaV_4S_8 . In Fig. 2 we present the phase diagram of GaV_4S_8 based on magnetization, magneto- and pyrocurrent as well as on specific-heat measurements for magnetic fields

applied along the crystallographic $\langle 111 \rangle$ direction (a phase diagram based on magnetization measurements alone was published in ref. 14). In GaV_4S_8 due to easy-axis exchange anisotropy, the skyrmion cores are always aligned parallel to the $\langle 111 \rangle$ easy axis and they are not oriented by low external magnetic fields. Therefore, when the magnetic field is applied along $\langle 111 \rangle$, one magnetically favourable domain coexists with three unfavourable domains, whose cycloidal and SkL states persist up to higher fields¹⁴. The finite electric polarization measured without poling electric fields indicates unequal domain population. Moreover, since its value does not change after several warming-cooling cycles, we assume that the unique domain, i.e. the polarization monodomain state, is stabilized in the present experiment. Therefore, in Fig. 2 we focus on the low-field phase diagram specific to this domain, neglecting the cycloidal and SkL phases occurring at higher fields in the magnetically unfavourable domains¹⁴.

Figure 2a presents the magnetic-field versus temperature phase diagram of GaV_4S_8 for $T < 15$ K, while Fig. 2b shows the complete H-T phase diagram extending beyond the Jahn-Teller transition. Below the magnetic phase transition, occurring at $T_C = 13$ K, two magnetic-phase pockets, the cycloidal and the SkL phases, are embedded in the FM phase¹⁴. In zero magnetic field, the FM, the cycloidal and the orbitally ordered PM phases are all ferroelectric as evidenced by Fig. 1d (denoted in Fig. 2 as FE2, FE3 and FE1, respectively). The orbitally disordered phase above $T_{JT} = 44$ K is a PM semiconductor without FE polarization.

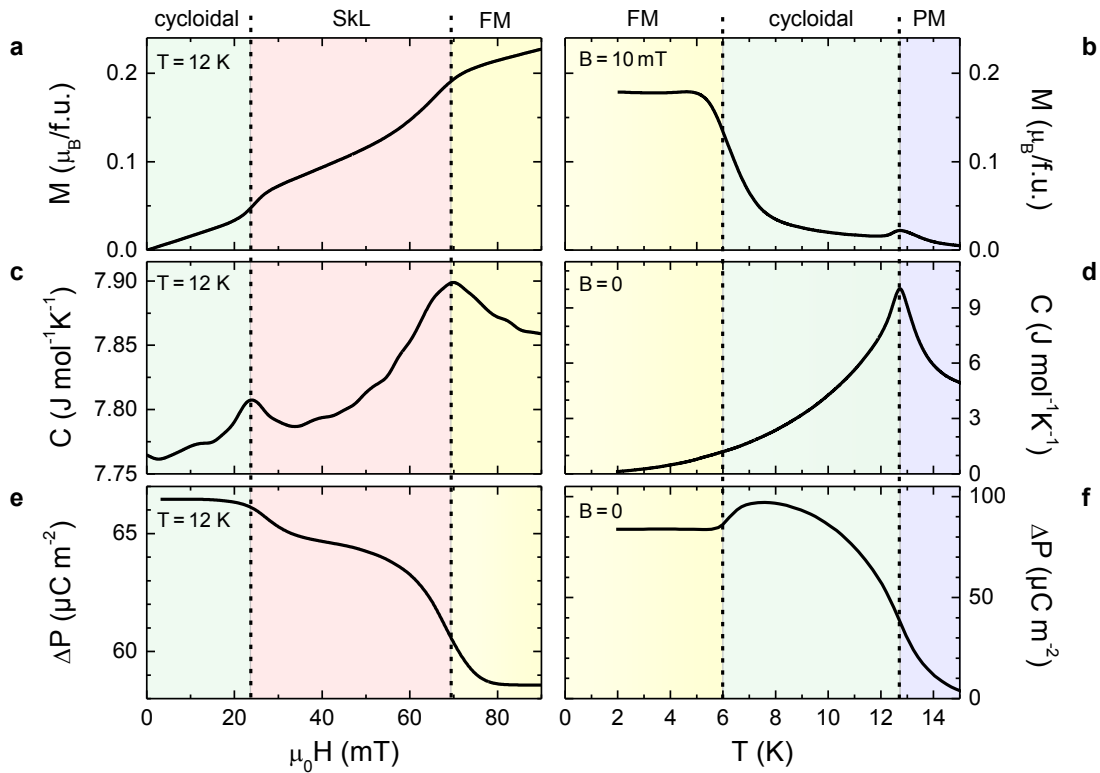


Figure 3 | Anomalies in magnetization, specific heat and FE polarization at the magnetic phase boundaries. (a),(c),(e) Magnetic-field dependence of magnetization (M), specific heat (C) and isothermal polarization (ΔP) with $H \parallel \langle 111 \rangle$. (b),(d),(f) Temperature dependence of magnetization, specific heat and zero-field polarization. Background colours represent the different magnetic phases following the colour code used in Fig. 2.

To further elucidate the phase diagram (Fig. 2a), a representative set of magnetization, specific heat and polarization curves as function of temperature and magnetic field are shown in Fig. 3. At the phase boundaries clear anomalies can be identified in the field dependent (Figs. 3a,c,e), as well as in the temperature dependent scans (b,d,f) of all three quantities. The only exception is the temperature

dependence of the heat capacity (Fig. 3d) which reveals no anomaly when passing from the cycloidal to the ferromagnetic phase, indicating negligible changes in entropy. The position of all observed anomalies are included in Fig. 2a, which are in perfect agreement with each other and the published phase boundaries¹⁴ and, thus, convincingly document the complexity of the low-temperature phase diagram of GaV₄S₈. It has to be noted that the excess spin-driven polarization ΔP at the magnetic phase boundaries, as presented in Figs 3e and 3d, appears on top of a much larger orbital-order derived polarization (see Fig. 1d).

Ferroelectricity in the magnetic phases. To obtain more detailed information about the different FE phases, including the SkL phase, we studied the temperature (Fig. 4) and field dependence (Fig. 5) of the FE polarization deduced from pyro- and magnetocurrent measurements, respectively. In all scans presented in Figs. 3-5, only the excess polarizations of the magnetic phases are shown, which are less than 2% of the orbitally-derived ferroelectricity emerging at T_{JT} (see inset in Fig. 1d).

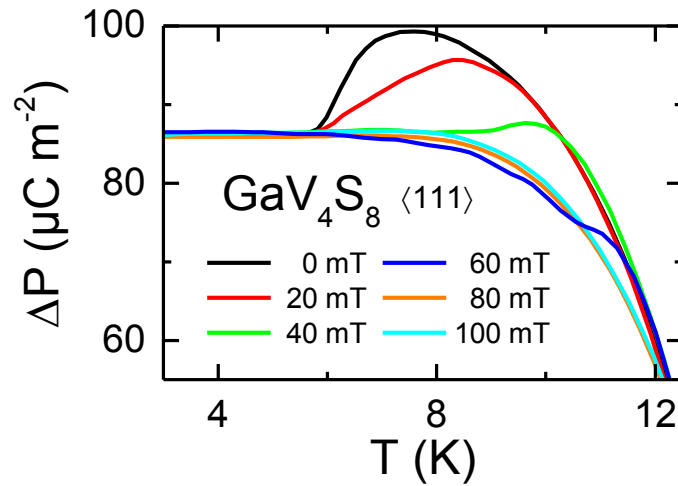


Figure 4 | Ferroelectric polarization of GaV₄S₈ determined from pyrocurrent measurements. The figure shows the polarization as function of temperature measured in various magnetic fields between 0 and 100 mT. Only the excess polarization ΔP , arising when entering the magnetic phases at $T_c = 13$ K, is shown.

Fig. 4 shows the temperature dependence of the excess polarization ΔP in various magnetic fields between 0 and 100 mT, while Fig. 5 presents the polarization versus magnetic field at temperatures between 2 and 13 K. The steps observed in the field and temperature dependence of the polarization, corresponding to peaks in the magneto- and pyrocurrent curves, are indicated in Fig. 2a by open and closed circles, respectively. They nicely match the phase boundaries determined from specific heat and magnetization data. All magnetically ordered phases are characterized by different excess polarizations. In fields of $\mu_0 H = 100$ mT, the material undergoes a PM to FM transition at $T_c = 13$ K without any intermediate phase, and the excess polarization in the FM phase reaches the saturation value, $\Delta P_{FM} \sim 86 \mu\text{C}/\text{m}^2$ at the lowest temperatures (see Fig. 4). The curves measured in $\mu_0 H = 0$ mT and 20 mT, following a steep increase at 13 K, exhibit an additional drop at about 6 K, where the transition from the cycloidal to FM phase takes place (see Fig. 2). Therefore, the polarization in the cycloidal phase is enhanced by approximately $14 \mu\text{C}/\text{m}^2$ compared to the purely FM collinear spin arrangement, resulting in a total excess polarization of $\Delta P_{cyc} \sim 100 \mu\text{C}/\text{m}^2$. The SkL to FM phase boundary is also accompanied by small but significant anomalies as revealed by the polarization curves measured in $\mu_0 H = 40$ and 60 mT (Fig. 4). Indeed, in Fig. 5 the magnetic-field dependent polarization curves recorded at temperatures between 10 K and 12 K show two subsequent steps which prove that the cycloidal, SkL and FM phase exhibit different excess polarizations. Summarizing the spin-derived ferroelectric excess polarizations as documented in Figs. 4 and 5, we find a saturation polarization of $86 \mu\text{C}/\text{m}^2$ for the collinear FM state from the temperature scan at 100 mT. The scan in zero field, crossing the cycloidal phase between 6 and 13 K results in $\Delta P_{cyc} \sim 100 \mu\text{C}/\text{m}^2$, while the scan at 40 mT, only crossing the SkL between 8 and 13 K, reveals an extra contribution of about

$5 \mu\text{C}/\text{m}^2$, resulting in $\Delta P_{SkL} \sim 91 \mu\text{C}/\text{m}^2$. This hierarchy of polarization also becomes evident from the isothermal scans in Fig. 5: At $T = 10.5 \text{ K}$ and for increasing magnetic fields, the polarization drops from approximately $87 \mu\text{C}/\text{m}^2$ in the cycloidal phase, to $82 \mu\text{C}/\text{m}^2$ in the SkL phase and finally to $73 \mu\text{C}/\text{m}^2$ in the FM state.

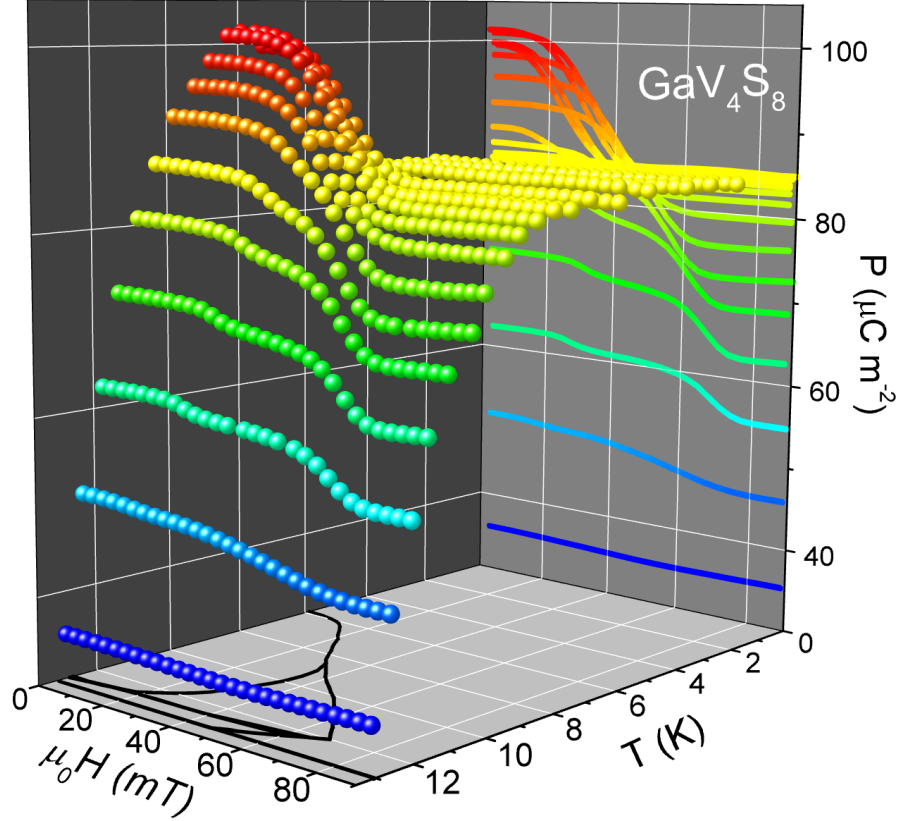


Figure 5 | Ferroelectric polarization of GaV_4S_8 determined from magnetocurrent measurements. Magnetic field dependence of the isothermal polarization measured at various temperatures between 2 and 13 K. Only the excess polarization, ΔP , induced by the magnetic ordering is shown. A step-like increase of the polarization at the transition from the cycloidal to SkL and from the SkL to the FM phase can be identified in the $P(H)$ curves measured between 7 and 12.5 K. All the $P(H)$ curves are projected onto the H - P plane and all phase boundaries are indicated in the H - T plane of the figure. The black lines on the H - T plane indicate the same magnetic phase boundaries as in Fig. 2a.

It is interesting to compare the spin-derived polarization in the Néel-type skyrmion host GaV_4S_8 with that observed in Cu_2OSeO_3 with Bloch-type skyrmions. In Cu_2OSeO_3 , which is the only insulating material reported to host a SkL state so far, the polarization varies in the range of $\pm 0.5 \mu\text{C}/\text{m}^2$ in the helical and SkL phase^{23,32,33}. This is significantly lower than the polarizations observed in the lacunar spinel compound investigated in the present study. Another important difference is that, while in the helical and FM phase of Cu_2OSeO_3 the FE polarization continuously increases with increasing external magnetic field and is zero for zero magnetic field,²³ well developed excess-polarization plateaus are detected in all magnetic phases of GaV_4S_8 , even in the absence of external magnetic fields (see Fig. 5). This fact documents that the excess polarization in GaV_4S_8 is spin-driven and appears spontaneously at the magnetic phase boundaries, while the polarization in Cu_2OSeO_3 is induced by external magnetic fields only and follows a quadratic magnetoelectric coupling.²³

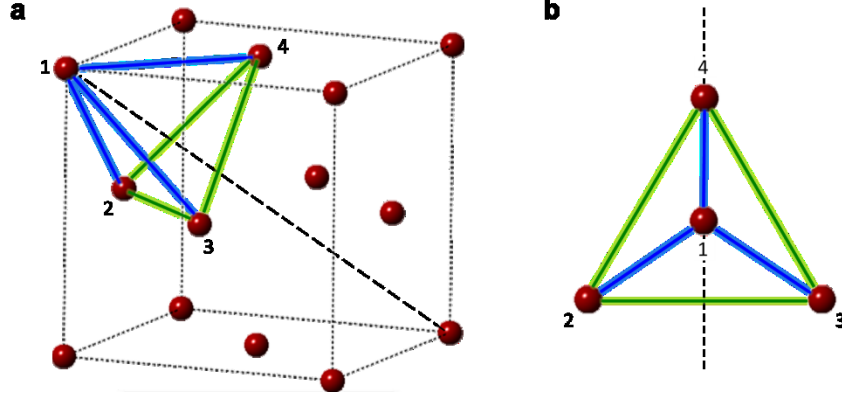


Figure 6 | Bond symmetry in the rhombohedrally distorted structure of GaV₄S₈. (a) V₄ clusters (represented by red spheres) form an fcc lattice stretched along one of the body diagonals (dashed line). Due to this distortion, there are two types of bonds as illustrated for four selected clusters: Intra-plane ones (green lines) between nearest neighbour V₄ units within the (111) planes and inter-plane ones (blue lines) connecting V₄ units in neighbouring (111) planes. (b) The four selected clusters viewed from the $\langle 111 \rangle$ direction. Each blue bond lies within a mirror plane of the tetrahedron (see dashed line for an example), while green bonds are perpendicular to them.

Microscopic origin of the spin-driven polarization. Motivated by the distinct values of the spin-driven polarization in the cycloidal, SkL and FM phase, we analyse its microscopic origin taking into account the rhombohedral symmetry of the lattice and the spin patterns in the three magnetically ordered phases. The building blocks of the magnetic structure, that are the V₄ tetrahedra with $S = 1/2$, form an fcc lattice elongated parallel to one of the $\langle 111 \rangle$ axes. Due to this distortion, the bonds between nearest neighbour V₄ units within the (111) planes are not equivalent with those connecting V₄ units in neighbouring (111) planes as illustrated in Fig. 6. Hereafter, these bonds are referred to as intra- and inter-plane bonds, respectively.

In general, the spin-driven excess polarization, ΔP , can be written as a sum of the polarization of individual bonds being bilinear function of spin components:

$$\Delta P^\alpha = \frac{1}{N} \sum_{\substack{\langle i,j \rangle \\ \beta,\gamma}} \lambda_{i,j}^{\alpha\beta\gamma} S_i^\beta S_j^\gamma, \quad (1)$$

where the summation goes over all β and γ spin components for each $\langle i,j \rangle$ bond. Since GaV₄S₈ is an $S = 1/2$ cluster-spin system, the on-site ($i=j$) polarization terms can be neglected. The form of the magnetoelectric coupling tensors $\lambda_{i,j}^{\alpha\beta\gamma}$ are bond specific and dictated by the symmetry of the bonds^{34,35}. In the experiment only ΔP^z was detected, where the z axis points along $\langle 111 \rangle$. Hence, we will restrict our analysis to the second-rank tensors $\lambda_{i,j}^{(z)\beta\gamma}$ and will omit the z index. (Here we note that due to the presence of FE polarization in the PM phase, $\lambda_{i,j}^{\beta\gamma}$ has the same form, i.e. the same independent non-zero elements, as the exchange coupling matrix $J_{i,j}^{\beta\gamma}$.) As shown in Fig. 6, the intra-plane bonds are perpendicular to the mirror planes present in C_{3v} symmetry, while the inter-plane bonds lie within these mirror planes. Correspondingly, the magnetoelectric coupling tensors for a selected intra- and inter-plane bond in Fig. 6b have the forms:

$$\hat{\lambda}_{2,3} = \begin{bmatrix} \lambda^{xx} & \lambda^{xy} & \lambda^{xz} \\ -\lambda^{xy} & \lambda^{yy} & \lambda^{yz} \\ -\lambda^{xz} & \lambda^{yz} & \lambda^{zz} \end{bmatrix}, \quad \hat{\lambda}_{1,4} = \begin{bmatrix} \Lambda^{xx} & 0 & 0 \\ 0 & \Lambda^{yy} & \Lambda^{yz} \\ 0 & \Lambda^{zy} & \Lambda^{zz} \end{bmatrix}. \quad (2)$$

The symmetric and antisymmetric part of the tensors describes the polarization generated by the exchange-striction and spin-current mechanism, respectively^{29,34,36}. The form of $\hat{\lambda}$ matrices for the other bonds can be derived by applying 3-fold rotations.

Next, we calculate the uniform component of ΔP_z in the magnetically ordered phases using the magnetoelectric coupling tensors described in Eq. (2). Since the wavelength of the magnetic modulation ($2\pi/q$) is more than 20 times larger than the lattice constant a in both the cycloidal and SkL phase¹⁴, we use the continuum approximation when describing their spin patterns:

$$\mathbf{S}_{\text{cyc}}(\mathbf{r}) = \frac{1}{2} [a_1 \Re\{\mathbf{S}_j e^{i\mathbf{q}_j \mathbf{r}}\} + \text{higher harmonics}], \quad (3a)$$

$$\mathbf{S}_{\text{SkL}}(\mathbf{r}) = \frac{1}{2} \left[b_0 \mathbf{S}_0 + b_1 \sum_{j=1}^3 \Re\{\mathbf{S}_j e^{i\mathbf{q}_j \mathbf{r}}\} + \text{higher harmonics} \right], \quad (3b)$$

$$\mathbf{S}_{\text{FM}}(\mathbf{r}) = \frac{1}{2} c_0 \mathbf{S}_0, \quad (3c)$$

where the propagation vectors of magnetic order are $\mathbf{q}_1 = q(1,0,0)$, $\mathbf{q}_2 = q(-\frac{1}{2}, \frac{\sqrt{3}}{2}, 0)$, $\mathbf{q}_3 = q(-\frac{1}{2}, -\frac{\sqrt{3}}{2}, 0)$ and the corresponding Fourier components are $\mathbf{S}_j = \mathbf{S}_0 - i\mathbf{q}_j/q$ with $\mathbf{S}_0 = (0,0,1)$. In zero magnetic field, we assume that the cycloid has only the fundamental harmonic, i.e. $a_i = 0$ for $i > 1$, which is valid when the magnetic anisotropy is small. The SkL can also be expressed as a Fourier series, where each order contains a superposition of three cycloids whose \mathbf{q} -vectors sum up to zero. In first order, these are the three fundamental harmonics with \mathbf{q}_1 , \mathbf{q}_2 and \mathbf{q}_3 . Higher order terms are necessary to keep the spin length constant. The coefficients a_j , b_j and c_0 depend on the temperature and magnetic field. The uniform component of the polarization can directly be obtained by substituting Eqs. (2) and (3) into Eq. (1) and integrating over the area of the magnetic unit cell of the respective phases:

$$\Delta P_{\text{cyc}} \approx \frac{3}{16} a_1^2 \left[(\lambda^{zz} + \Lambda^{zz}) + \sum_{\alpha} (\lambda^{\alpha\alpha} + \Lambda^{\alpha\alpha}) \right], \quad (4a)$$

$$\Delta P_{\text{SkL}} \approx \frac{3}{4} b_0^2 (\lambda^{zz} + \Lambda^{zz}) + \frac{9}{16} \sum_{i=1}^3 b_i^2 \left[(\lambda^{zz} + \Lambda^{zz}) + \sum_{\alpha} (\lambda^{\alpha\alpha} + \Lambda^{\alpha\alpha}) \right], \quad (4b)$$

$$\Delta P_{\text{FM}} \approx \frac{3}{4} c_0^2 (\lambda^{zz} + \Lambda^{zz}). \quad (4c)$$

All the polarization terms above come from the exchange-striction mechanism. We assume that contributions from the spin-current mechanism, corresponding to the asymmetric parts of the $\hat{\lambda}$ matrices, can be neglected even in the non-collinear cycloidal and SkL phase due to the slow spatial variation of these magnetic patterns. Additional contributions to the polarization arising from higher harmonics in the cycloidal and SkL state are governed by the strength of the weak exchange anisotropy, $\frac{\delta J}{J} = \frac{2(J^{zz} - J^{xx})}{(J^{xx} + J^{zz})} \approx 0.05$, i.e. reduced by the factor of $\delta J/J$ relative to the leading terms in Eqs. (4a) and (4b).

Reflecting the axial symmetry in the rhombohedral phase, the polarization in leading order can be expressed by two parameters of the $\hat{\lambda}$ matrices, namely the sum of their zz elements, $(\lambda^{zz} + \Lambda^{zz})$, and the sum of their traces, $\sum_{\alpha} (\lambda^{\alpha\alpha} + \Lambda^{\alpha\alpha})$. Next, we determine these parameters based on the measured excess polarizations of cycloidal and FM phase, assuming that the ordered moment in the FM ground state and the low-temperature region of the cycloidal phase is close to $S = \frac{1}{2}$, i.e. $a_1 \approx c_0 \approx 1$. With $\Delta P_{\text{cyc}} = 100 \mu\text{C}/\text{cm}^2$ and $\Delta P_{\text{FM}} = 86 \mu\text{C}/\text{cm}^2$ we obtain $(\lambda^{zz} + \Lambda^{zz}) = 115 \mu\text{C}/\text{cm}^2$ and $\sum_{\alpha} (\lambda^{\alpha\alpha} + \Lambda^{\alpha\alpha}) = 418 \frac{\mu\text{C}}{\text{cm}^2}$. Detailed description of the spin structure in the SkL phase, i.e. the exact values of the b_n coefficients in Eq. (4b), are not available, thus, for the visualization of the spatial dependence of the FE polarization we employ the following model of a single skyrmion³⁷:

$$\mathbf{S}_{\text{Sk}}(\mathbf{r}) = \frac{1}{2} \begin{bmatrix} \frac{2\xi x}{x^2 + y^2 + \xi^2} \\ \frac{2\xi y}{x^2 + y^2 + \xi^2} \\ \frac{x^2 + y^2 - \xi^2}{x^2 + y^2 + \xi^2} \end{bmatrix}, \quad (5)$$

where ξ is the effective radius of the skyrmion core. The z component of the spins changes sign at this radius when moving from the centre to the edge of the skyrmion. The spatial dependence of the z component of the spin-driven polarization reads as

$$\Delta P_{\text{Sk}} \approx \frac{3}{2} \left[\frac{4\xi^2(x^2 + y^2)}{(x^2 + y^2 + \xi^2)^2} \frac{\lambda^{xx} + \Lambda^{xx} + \lambda^{yy} + \Lambda^{yy}}{2} + \frac{(x^2 + y^2 - \xi^2)^2}{(x^2 + y^2 + \xi^2)^2} (\lambda^{zz} + \Lambda^{zz}) \right]. \quad (6)$$

Figure 7 shows the corresponding spatial dependence of the z component of the spin and the polarization. For the magnitude of the magnetoelectric coefficients $\hat{\lambda}$ in Eq. (6), we use the values determined above from the analysis of the cycloidal and FM phases. The characteristic ring like pattern of the z component of the polarization and its strong spatial modulation in the vicinity of the skyrmion core, as high as 25 - 30%, should allow the experimental observation of this nanoscale multiferroic structure.

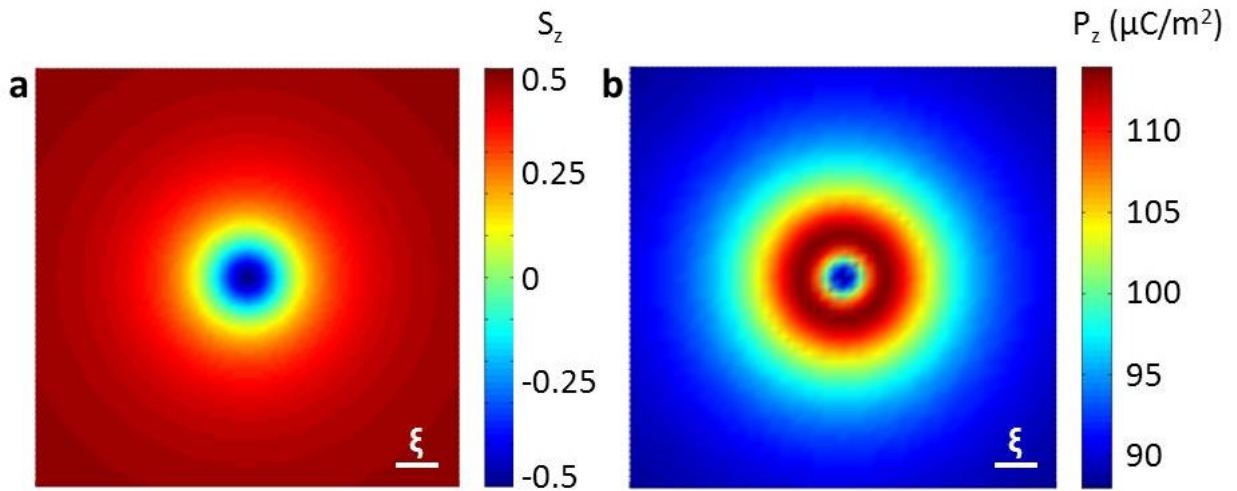


Figure 7 | Polar dressing of the SkL in GaV₄S₈. (a) Spatial dependence of the z component of the $S = 1/2$ spins forming the skyrmion and (b) spatial dependence of the spin-driven polarization \mathbf{P}_z , both in the xy plane perpendicular to the vortex core. The radius of the skyrmion core, ξ , sets the lateral length scale. The polarization reaches its maximum in a ring-like region around the skyrmion cores (red regions). The outer blue regions in the polarization indicate the FE polarization of the almost collinear spin arrangement at the outer rims of the skyrmion.

Discussion

In the present work we have identified four different FE phases in the magnetic semiconductor GaV₄S₈. The large polarization of about 6000 $\mu\text{C}/\text{m}^2$ in the FE1 phase, which appears below the Jahn-Teller transition, likely originates from ionic displacements driven by the ferro-orbital order and is further enhanced when entering the magnetically ordered phases at low temperatures. The excess polarization of the FE2 phase with collinear FM order is about 90 $\mu\text{C}/\text{m}^2$. The non-collinear spin patterns in the cycloidal and SkL phase further enhance the FE polarization and all multiferroic phases, FE2, FE3 and FE4, can be characterized by three distinct levels of the excess polarization. The four FE phases, out of which three are also magnetically ordered, points to a complex entanglement of polar, orbital and magnetic degrees of freedom in the lacunar spinel GaV₄S₈. Most importantly we

observe ferroelectric skyrmions with a strong spatial modulation of the FE polarization in the vicinity of the skyrmion core.

We argue that the spin-driven polarization is dominated by the exchange-striction mechanism in each multiferroic phase, while the spin-current and spin-dependent orbital hybridization mechanism play minor roles due to the slow spatial variation of the spin patterns and the $S = \frac{1}{2}$ spins of the V_4 clusters, respectively. We have studied the origin of the magnetoelectric effect on the microscopic level by analysing the symmetry of the V_4 - V_4 bonds in the rhombohedral phase and determined the two sets of magnetoelectric coefficients responsible for the spin-driven polarization.

The excess polarization in the SkL phase of GaV_4S_8 is almost two orders of magnitude larger than that of Cu_2OSeO_3 , the only magnetoelectric skyrmion-host material known so far. This sizable polarization may offer an efficient electric control of the SkL state as already demonstrated in Cu_2OSeO_3 ³⁸, which would be an important step in the development of skyrmion-based memory devices^{39,40,41,42}. This ambitious goal requires, at the first stage, the nano-scale observation of the polar pattern associated with the SkL using local probes such as scanning force and Kelvin-probe microscopy^{43,44,45}.

Methods

Polycrystalline GaV_4S_8 was prepared by solid state reaction using pure elements of Ga (6N), V (3N) and S (5N). Three subsequent synthesis steps were necessary to obtain full reaction of the starting materials to form the stoichiometric ternary phase. Phase purity after each step was checked by x-ray powder diffraction. The synthesized polycrystals were used as starting material for single crystal growth using chemical transport reactions. The growth was performed in closed quartz ampoules at temperatures between 800 and 850°C utilizing iodine as transport agent. Crushed single crystals have been characterized by x-ray diffraction and were found to be free of any impurity phases. At room temperature we found the correct $GaMo_4S_8$ -type structure with F-43m symmetry and a lattice constant $a = 0.966$ nm. Magnetic measurements were performed with a SQUID magnetometer (Quantum Design MPMS XL) in the temperature range from 1.8 K $< T < 400$ K and in external magnetic fields up to 5 T. The heat capacity was investigated in a Physical Properties Measurement System (Quantum Design PPMS) for temperatures 1.8 K $< T < 300$ K. The dielectric experiments were performed with a Novocontrol Alpha-Analyzer in a frequency range from 1 Hz to 10 MHz and the pyrocurrent has been measured utilizing the Keithley Electrometer 6517A as a function of temperature between 2 and 55 K. In addition we measured the magnetocurrent at temperatures between 2 K and 14 K and in external fields between 0 and 300 mT. In these experiments we used platelet-shaped single crystals of size of 1 mm² and 0.25 mm thickness. The large (111) surfaces of these samples were contacted by silver paste.

References

1. Barz, H. New ferromagnetic molybdenum spinels. *Mat. Res. Bull.* **8**, 983-988 (1973).
2. Perrin, C., Chevrel, M. R. & Sergent, M. New tetrahedral clusters of molybdenum in chalcogenides MMo_4S_8 (M=Al,Ga), $GaMo_4Se_8$ and Thiohalides $MoSX$ (X=Cl, Br, I). *C. R. Acad. Sc. Paris* **280**, 949-951 (1975).
3. Brasen, D. *et al.* Magnetic and crystallographic properties of spinels of the type $A_xB_2S_4$ where A = Al, Ga, and B = Mo, V, Cr. *J. Sol. Stat. Chem.* **13**, 298-303 (1975).
4. Müller, H., Kockelmann, W. & Johrendt, D. The magnetic structure and electronic ground states of Mott insulators GeV_4S_8 and GaV_4S_8 . *Chem. Mater.* **18**, 2174-2180 (2006).
5. Abd-Elmeguid, M. M. *et al.* Transition from Mott insulator to superconductor in $GaNb_4Se_8$ and $GaTa_4Se_8$ under high pressure. *Phys. Rev. Lett.* **93**, 126403 (2004).
6. Ta Phouc, V. *et al.* Optical conductivity measurements of $GaTa_4Se_8$ under high pressure: Evidence of a bandwidth-controlled insulator-to-metal Mott transition. *Phys. Rev. Lett.* **110**, 037401 (2013).
7. Camjayi, A. *et al.* First-order insulator-to-metal Mott transition in the paramagnetic 3D system $GaTa_4Se_8$. *Phys. Rev. Lett.* **113**, 086404 (2014).
8. Dorolti, E. *et al.* Half-Metallic Ferromagnetism and large negative magnetoresistance in the new lacunar spinel $GaTi_3VS_8$. *J. Am. Chem. Soc.* **132**, 5704-5710 (2010).
9. Kim, H.-S., Im, J., Han, M. J. & Jin, H. Spin-orbital entangled molecular j_{eff} states in lacunar spinel compounds. *Nat. Commun.* **5**, 3988 (2014).
10. V. Dubost *et al.* Resistive switching at the nanoscale in the Mott insulator compound $GaTa_4Se_8$. *Nano Letters* **13**, 3648-3653 (2013).

11. Stoliar, P. *et al.* Universal electric-field-driven resistive transition in narrow-gap Mott insulators. *Adv. Mater.* **25**, 3222-3226 (2013).
12. Guiot, V. *et al.* Avalanche breakdown in GaTa₄Se_{8-x}Te_x narrow-gap Mott insulators. *Nat. Commun.* **4**, 1722 (2013).
13. Singh, K. *et al.* Orbital-ordering-driven multiferroicity and magnetoelectric coupling in GeV₄S₈. *Phys. Rev. Lett.* **113**, 137602 (2014).
14. Kézsmárki, I. *et al.* Néel-type skyrmion lattice with confined orientation in the polar magnetic semiconductor GaV₄S₈. Preprint at <http://arxiv.org/abs/1502.08049> (2015).
15. Powell, A. V. *et al.* Cation Substitution in Defect Thiospinels: Structural and Magnetic Properties of GaV_{4-x}Mo_xS₈ (0 ≤ x ≤ 4). *Chem. Mater.* **19**, 5035-5044 (2007).
16. Pocha, R., Johrendt, D. & Pöttgen, R. Electronic and structural instabilities in GaV₄S₈ and GaMo₄S₈. *Chem. Mater.* **12**, 2882-2887 (2000).
17. Sahoo Y. & Rastogi, A. K. Evidence of hopping conduction in the V₄-cluster compound GaV₄S₈. *J. Phys.: Condens. Matter* **5**, 5953-5962 (1993).
18. Yadav, C. S., Nigam, A. K. & Rastogi, A. K. Thermodynamic properties of ferromagnetic Mott-insulator GaV₄S₈. *Physica B* **403**, 1474-1475 (2008).
19. Nakamura, H., Chudo, H. & Shiga, M. Structural transition of the tetrahedral metal cluster: nuclear magnetic resonance study of GaV₄S₈. *J. Phys. Condens. Matter* **17**, 6015-6024 (2005).
20. Rössler, U. K., Bogdanov, A. N. & Pfleiderer, C. Spontaneous skyrmion ground states in magnetic metals. *Nature* **442**, 797-801 (2006).
21. Mühlbauer, S. *et al.* Skyrmion lattice in a chiral magnet. *Science* **323**, 915-919 (2009).
22. Yu, X. Z. *et al.* Real-space observation of a two-dimensional skyrmion crystal. *Nature* **465**, 901-904 (2010).
23. Seki, S., Yu, X. Z., Ishizawa, S. & Tokura, Y. Observation of skyrmions in a multiferroic material. *Science* **336**, 198-201 (2012).
24. Leonov, A. O. & Mostovoy, M. Multiply periodic states and isolated skyrmions in an anisotropic frustrated magnet. <http://arxiv.org/abs/1501.02757> (2015).
25. Malik, V., Yadav, C. S., Rastogi, A. & Kumar, D. Peculiar magnetism of transition metal cluster compounds. *Europhys. Lett.* **101**, 67008 (2013).
26. Lunkenheimer, P. *et al.* Origin of apparent colossal dielectric constants. *Phys. Rev. B* **66**, 052105 (2002).
27. Lunkenheimer, P. *et al.* Colossal dielectric constants in transition-metal oxides. *Eur. Phys. J. Special Topics* **180**, 61-89 (2010).
28. Kimura, T. *et al.* Magnetic control of ferroelectric polarization. *Nature* **426**, 55-58 (2003).
29. Cheong, S.-W. & Mostovoy, M. Multiferroics: a magnetic twist for ferroelectricity. *Nature Materials* **6**, 13-20 (2007).
30. Tokura, Y., Seki, S. & Nagaosa, N. Multiferroics of spin origin. *Rep. Prog. Phys.* **77**, 076501 (2014).
31. Merz, W. J. Double hysteresis loop of BaTiO₃ at the Curie point. *Phys. Rev.* **91**, 513-517 (1953).
32. Maisuradze, A., Shengelaya, A., Berger, H., Djokić, D. M. & Keller, H. Magnetoelectric Coupling in Single Crystal Cu₂OSeO₃ Studied by a Novel Electron Spin Resonance Technique. *Phys. Rev. Lett.* **108**, 247211 (2012).
33. Omrani, A. A. *et al.* Exploration of the helimagnetic and skyrmion lattice phase diagram in Cu₂OSeO₃ using magnetoelectric susceptibility. *Phys. Rev. B* **89**, 064406 (2014).
34. Jia, C., Onoda, S., Nagaosa, N. & Han, J. H. Microscopic theory of spin-polarization coupling in multiferroic transition metal oxides. *Phys. Rev. B* **76**, 144424 (2007).
35. Kaplan, T. A. & Mahanti, S. D. Canted-spin-caused electric dipoles: A local symmetry theory. *Phys. Rev. B* **83**, 174432 (2011).
36. Katsura, H., Nagaosa, N. & Balatsky, A. V. Spin Current and Magnetoelectric Effect in Noncollinear Magnets. *Phys. Rev. Lett.* **95**, 057205 (2005).
37. Sondhi, S. L., Karlhede, A., Kivelson, S. A. & Rezayi, E. H. Skyrmions and the crossover from the integer to fractional quantum Hall effect at small Zeeman energie. *Phys. Rev. B* **47**, 16419-16426 (1993).
38. White, J. S. *et al.* Electric-Field-Induced Skyrmion Distortion and Giant Lattice Rotation in the Magnetoelectric Insulator Cu₂OSeO₃. *Phys. Rev. Lett.* **113**, 107203 (2014).
39. Fert, A., Cros, V. & Sampaio, J. Skyrmions on the track. *Nat. Nanotechnol.* **8**, 152-156 (2013).
40. N. Nagaosa & Tokura, Y. Topological properties and dynamics of magnetic skyrmions. *Nat. Nanotechnol.* **8**, 899-911 (2013).
41. Sampaio, J., Cros, V., Rohart, S., Thiaville, A. & Fert, A. Nucleation, stability and current-induced motion of isolated magnetic skyrmions in nanostructures. *Nat. Nanotechnol.* **8**, 839-844 (2013).
42. M. Mochizuki *et al.* Thermally driven ratchet motion of a skyrmion microcrystal and topological magnon Hall effect. *Nat. Mater.* **13**, 241-246 (2014).
43. Saurenbach, F. & Terris, B. D. Imaging of ferroelectric domain walls by force microscopy. *Appl. Phys. Lett.* **56**, 1703-1705 (1990).
44. Eng, L. M. Nanoscale domain engineering and characterization of ferroelectric domains. *Nanotechnology* **10**, 405-411 (1999).
45. Kawai, S. *et al.* Atom manipulation on an insulating surface at room temperature. *Nat. Commun.* **5**, 4403 (2014).

Acknowledgements

This research was supported by the DFG via the Transregional Research Collaboration TRR 80: From electronic correlations to functionality (Augsburg/Munich/Stuttgart) and by the Hungarian Research Funds OTKA K 108918, OTKA PD 111756 and Bolyai 00565/14/11.

Author contributions

I.K., A.L. and P.L. conceived and supervised the project. V.T. grew the high-quality single crystals. E.R. performed and analysed the dielectric measurements. S.W. performed and analysed the specific-heat measurements. S.B. and I.K. performed the calculations. A.L. wrote the paper with contributions from I.K and P.L. All authors discussed the results and commented on the manuscript.

Additional information

Competing financial interests: The authors declare no competing financial interests.